Simplified Controller Design Method for Digitally Controlled LCL-Type PWM Converter with Multi-resonant Quasi-PR Controller and Capacitor–Current–Feedback Active Damping

Yongcan Lyu[†] and Hua Lin[*]

[†*]State Key Laboratory of Advanced Electromagnetic Engineering and Technology,
School of Electrical and Electronic Engineering, Huazhong University of Science and Technology, Wuhan, China

Abstract

To track the sinusoidal current under stationary frame and suppress the effects of low-order grid harmonics, the multi-resonant quasi-proportional plus resonant (PR) controller has been extensively used for digitally controlled LCL-type pulse-width modulation (PWM) converters with capacitor–current–feedback active damping. However, designing the controller is difficult because of its high order and large number of parameters. Moreover, the computation and PWM delays of the digitally controlled system significantly affect damping performance. In this study, the delay effect is analyzed by using the Nyquist diagrams and the system stability constraint condition can be obtained based on the Nyquist stability criterion. Moreover, impact analysis of the control parameters on the current loop performance, that is, steady-state error and stability margin, identifies that different control parameters play different decisive roles in current loop performance. Based on the analysis, a simplified controller design method based on the system specifications is proposed. Following the method, two design examples are given, and the experimental results verify the practicability and feasibility of the proposed design method.

Key words: Active damping, Controller design, Digital control delay, LCL filter, Multi-resonant quasi-PR controller

I. INTRODUCTION

With the development of renewable energy and smart grid, energy storage systems (ESSs) have become increasingly interesting. ESSs could smooth the output power and decouple energy generation from demand [1]. As an interface between storage elements and the power grid, a voltage source pulse-width modulation (PWM) converter plays an important role in the single-stage and multistage power conversion systems (PCS) for ESSs [1], [2]. To smooth the injected currents, the conventional L filter is replaced by the LCL filter because of its better harmonic attenuation ability [3]-[10].

However, given the resonance hazard of the LCL filter, damping solutions are required to stabilize the system.

Two main methods are used to dampen resonance, namely, passive damping and active damping. However, active damping is more well known than passive damping because no additional power loss occurs [3]-[10]. Among the various active damping solutions, capacitor–current–feedback active damping is selected in this study because of its effectiveness, simple implementation, and extensive application [6]-[10]. Capacitor–current–feedback active damping is equivalent to a virtual resistor connected in parallel with the filter capacitor [5]. This conclusion is drawn by excluding the delay effect.

However, computation and PWM delays occur in the digitally controlled system. The computation delay is the interval between the sampling instant and duty ratio update instant. The PWM delay is caused by the zero-order hold effect, which keeps the duty ratio constant after it has been updated [10]-[13]. Given the delay effect, the capacitor–current–

feedback active damping is equivalent to a variable virtual impedance, which consists of a resistor connected in parallel with a reactor, rather than a virtual resistor. When the virtual resistor is negative, two unstable poles will be generated in the grid current loop [10]. As a result, the resonance peak should not be dampened to less than 0 dB to ensure system stability [8]. Thus, the capacitor–current–feedback gain should be selected with extreme caution.

In addition to system stability, high-quality injected power is another essential object in the control of the LCL-type PWM converter. Thus, the selection and design of the current controller is crucial. The stationary α–β frame is selected in this study to prevent the inconvenient decoupling in the synchronous d–q frame [6]. To track the sinusoidal current reference and suppress the selected low-order current harmonics, the proportional plus multifrequency resonant (multi-resonant proportional plus resonant [PR]) controller has been used extensively [14]-[19]. An ideal resonant controller can provide infinite gain to eliminate the steady-state error, but it occurs at the target frequency only. Any perturbation, such as frequency deviation, will lead to a significant reduction in the generated gain [18]. However, in fact, the grid frequency is allowed to deviate by ±0.5 Hz. Hence, the performance of the controller will be reduced, especially when applied to weak grids and microgrids where the frequency deviates even worse [20]. Moreover, attaining an ideal resonant controller is sometimes impossible because of finite precision in digital systems. To address these issues, the quasi-resonant controller is proposed [12], [19], [21]-[24]. The quasi-resonant controller can provide a sufficiently large gain around the target frequency to reduce its sensitivity to the grid frequency fluctuation and can be attained in digital platforms with a higher accuracy.

However, the design of the quasi-resonant controller, especially the multifrequency quasi-resonant controller (multi-resonant quasi-PR controller), is more difficult than that of the ideal resonant controller because the steady-state error should be taken into account in addition to stability and the stability margin. The design of a single quasi-PR controller is relatively easy and has been presented in [9], [12]. In general, the single quasi-PR controller can be designed based on steady-state error, crossover frequency (f_{cs}), phase margin (PM), and gain margin (GM) of the system, which have a significant effect on system performance and stability margin. However, these design methods are not applicable for the multi-resonant quasi-PR controller because calculating the PM of the controller is impossible because of its high order and large number of parameters. In [21], a guideline on designing the multifrequency quasi-resonant controller (without the proportional controller) is presented, which considered grid frequency deviation, grid synchronization, grid impedance variation, and transient response. In [24], pole placement is used to determine the controller parameters by properly
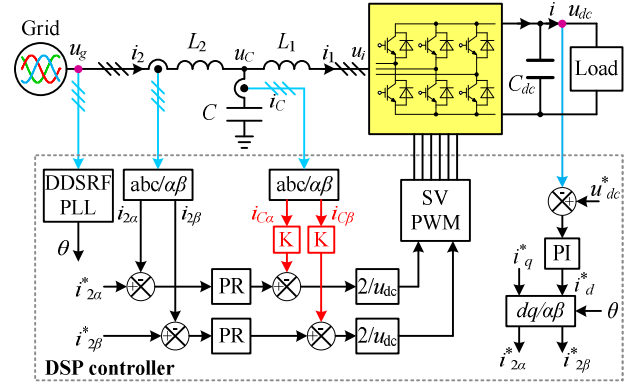

Fig. 1. Topology and control strategy of a three-phase LCL-type PWM converter in the stationary α–β frame.

selecting the poles to guarantee system stability and acceptable performance of the current loop. In [23], the controller parameters are designed separately mainly based on the requirements of the steady-state errors and PM. However, these design methods are inconvenient for engineers, and previous studies do not focus considerable attention on capacitor–current–feedback active damping.

The effect of computation and PWM delays on the active damping performance is analyzed in detail by using Nyquist diagrams. The effect of the controller parameters on the current loop performance with the application of frequency response theory in the continuous domain is also investigated. Then, a simplified practical design method of the multi-resonant quasi-PR controller and capacitor–current–feedback coefficient is proposed in this study. The paper is organized as follows: In Section II, the average switching model (ASM) of the internal current loop considering the control delay is derived. Based on the derived ASM, the effect of the delay on the active damping performance, which influences the stability constraint condition of the current loop, is investigated by using the Nyquist stability criterion in Section III. In Section IV, the effect of the control parameters on system performance, that is, system stability constraint condition, steady-state error, and stability margin, are investigated. Based on the analysis, a simplified design method is proposed in Section V, and two design examples are conducted step by step by using the proposed method. In Section VI, the effectiveness of the proposed design method is verified by using the experimental results from a prototype of a three-phase LCL-type PWM converter. The conclusion is given in Section VII.

II. CONTROL STRATEGY AND MODEL OF THE LCL-TYPE PWM CONVERTER

Fig. 1 shows the configuration of a three-phase LCL-type grid-connected PWM converter in the stationary α–β frame. The LCL filter is composed of L_1, C, and L_2. C_{dc} is the direct current (DC) link capacitor. As the equivalent series resistors
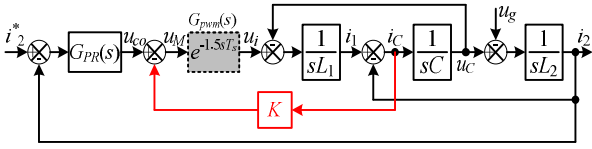
Fig. 2. Single-phase equivalent ASM of the current loop for the digitally controlled LCL-type PWM converter in inverter mode.
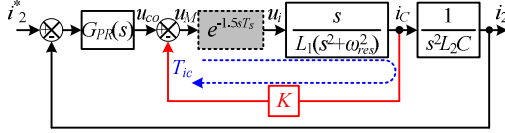

Fig. 3. Standard dual-loop structure of the grid current loop with capacitor current active damping.

(ESRs) of L_1, C, and L_2 can provide a certain degree of damping and help stabilize the system, the ESRs are omitted in this study to obtain the worst case.

As an interface between storage elements and the power grid in two-stage PCS, the primary objective of the PWM converter is to exchange power with the grid by controlling the grid current i_2 directly. To directly control the battery charge–discharge and prolong its service time, the DC link voltage u_{dc} is also controlled by the PWM converter. As such, the d-axis current reference is generated by the outer DC voltage loop. Thus, the α-axis and β-axis current references $i_{2\alpha\beta}^*$ are obtained by using the reverse Park transformation to the d-axis and q-axis current references i_{dq}^*. To synchronize with the grid voltage u_g, the phase angle of u_g is detected through a decoupled double synchronous reference frame phase-locked loop [25]. The capacitor current i_C serves as feedback to damp the LCL filter resonance actively, and K is the feedback coefficient. The capacitor–current–feedback signal is subtracted from the output of the current controller. Then, the capacitor–current–feedback signal is normalized with respect to $u_{dc}/2$ to obtain the modulation reference, which is fed to a digital PWM modulator.

As previously mentioned, computation and PWM delays occur in the digitally controlled system. The computation delay is one sampling period T_s in the synchronous sampling case when sampling is conducted at the beginning of a switching period. The calculated duty ratio is not updated until the next sampling instant. The PWM delay is definitely a half sampling period. Thus, the total delay is one and a half sampling periods ($1.5T_s$) [10]–[13]. The single-phase equivalent ASM of the current loop for the converter in inverter mode is shown in Fig. 2. We noted that the antialiasing filter could be removed in the synchronous sampling case [11]. Therefore, the grid current i_2 can be derived as follows:

$$i_2(s) = \frac{T(s)}{1+T(s)} i_2^*(s) - \frac{G_g(s)}{1+T(s)} u_g(s), \quad (1)$$

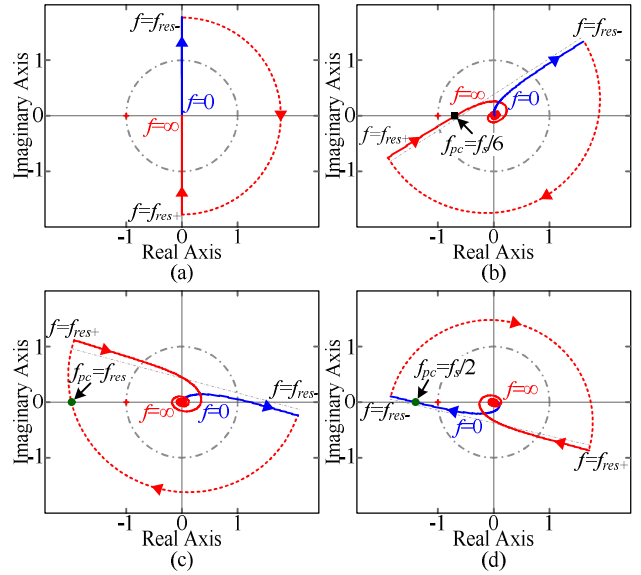where $T(s)$ is the loop gain of the system and is expressed as follows:

Fig. 4. Nyquist diagrams for the positive frequency of the active damping loop with different ω_{res}. (a) Analog control (no delay). (b) $\omega_s/6 > \omega_{res}$. (c) $\omega_s/6 \leq \omega_{res} \leq \omega_s/2$. (d) $\omega_s/2 < \omega_{res}$.

$$T(s) = G_{PR}(s) \cdot G_{LCL}(s)$$
$$= G_{PR}(s) \cdot \frac{\omega_{res}^2 e^{-1.5T_s s}}{s(L_1+L_2)\left(s^2 + se^{-1.5T_s s} K/L_1 + \omega_{res}^2\right)} \quad (2)$$

and $G_g(s)$ is expressed as follows:

$$G_g(s) = \frac{s^2 L_1 C + sKC e^{-1.5T_s s} + 1}{s^3 L_1 L_2 C + s^2 e^{-1.5T_s s} K L_2 C + s(L_1+L_2)}, \quad (3)$$

where $\omega_{res} = \sqrt{(L_1+L_2)/(L_1 L_2 C)}$ is the resonance angular frequency of the LCL filter.

As shown in Eq. (1), the grid voltage low-order harmonics have a significant effect on the grid current i_2. To suppress the effect of the low-order harmonics, the multi-resonant quasi-PR controller is employed. The transfer function is expressed as follows:

$$G_{PR}(s) = K_p + \sum_{h=1}^{m} \frac{2K_{rh}\omega_c s}{s^2 + 2\omega_c s + \omega_h^2}, \quad (4)$$

where h can take the values 1, 3, 5, 7, …, m, with m being the highest current harmonic to be attenuated.

III. EFFECT OF THE COMPUTATION AND PWM DELAYS ON THE ACTIVE DAMPING PERFORMANCE

As shown in Fig. 2, considering u_g as the disturbance, the block diagram can be transformed into the standard dual-loop structure shown in Fig. 3. The loop gain of the active damping loop $T_{ic}(s)$ can be derived as follows:

$$T_{ic}(s) = \frac{Ks}{L_1} \frac{e^{-1.5T_s s}}{s^2 + \omega_{res}^2}. \quad (5)$$

As shown in Fig. 3, the grid current loop $T(s)$ has no open-loop poles that lie in the right half plane (RHP), except for the active damping loop. That is to say, the number of RHP
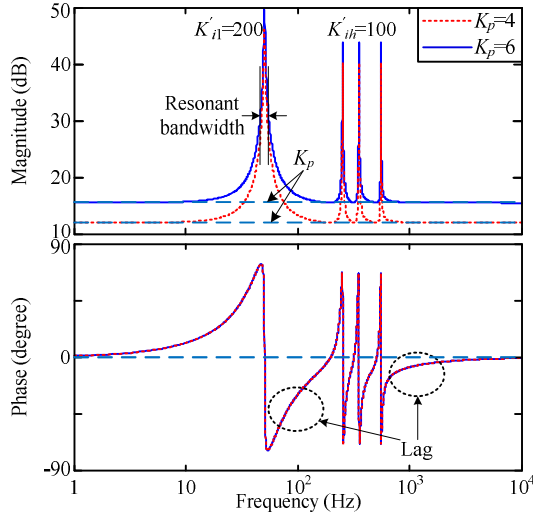
Fig. 5. Bode diagram of the multi-resonant quasi-PR controller ($\omega_c = 3$) with different parameters.

Fig. 6. Nyquist diagrams of the loop gain $T(s)$ with $G_{PR}(s) = K_p$. (a) $\omega_{res} < \omega_s/6$. (b) $\omega_{res} \geq \omega_s/6$.

closed-loop poles of the active damping loop determines the number of RHP open-loop poles of $T(s)$. In this study, the Nyquist diagram of $T_{ic}(s)$ is used to determine the number of RHP closed-loop poles by examining the magnitude at the negative real axis crossing frequency ω_{pc}. Notably, the crossing points at high frequencies caused by the delay effect affect stability only slightly. As such, the conclusions obtained on the delay effect are summarized as follows. Similar results can be found in [10].

1. If $0 < K < K_c$ when $\omega_{res} < \omega_s/6$, then $\omega_{pc} = \omega_s/6$ and $|T_{ic}(\omega_{pc})| < 1$, where ω_s is the sampling angular frequency and K_c, the critical value of K, is derived using Eq. (6) with $|T_{ic}(\omega_{pc})| = 1$. Accordingly, the Nyquist curve of $T_{ic}(s)$ does not encircle the critical point [see Fig. 4(b)]. Based on the Nyquist stability criterion, the active damping loop is stable and $T(s)$ has no RHP open-loop pole.

$$K_c = \frac{L_1}{\omega_s/6}\left[\left(\omega_s/6\right)^2 - \omega_{res}^2\right] \qquad (6)$$

2. If $K > K_c$ when $\omega_{res} < \omega_s/6$, then the crossing point in Fig. 4(b) is moved to the left of $(-1, j_0)$, that is, $|T_{ic}(\omega_{pc})| > 1$, and the Nyquist curve of $T_{ic}(s)$ will make one clockwise encirclement of the point $(-1, j_0)$. As such, the active damping loop is unstable with two generated RHP closed-loop poles, and $T(s)$ contains two RHP open-loop poles.

3. If $K > 0$ when $\omega_s/2 \geq \omega_{res} \geq \omega_s/6$, then $\omega_{pc} = \omega_{res}$, $|T_{ic}(\omega_{pc})| = \infty$, and the Nyquist curve always encircles the critical point once in the clockwise direction [see Fig. 4(c)]. Thus, the active damping loop is unstable with two RHP closed-loop poles, and $T(s)$ contains two RHP open-loop poles.

Notably, when $\omega_{res} > \omega_s/2$, the Nyquist curve may encircle the critical point [see Fig. 4(d)]. However, this case will never occur because $\omega_{res} < \omega_s/2$ is required to ensure system
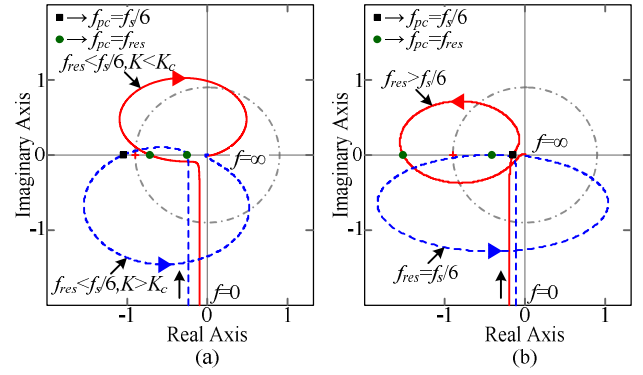
controllability [26].

IV. SYSTEM PERFORMANCE ANALYSIS

As shown in Eqs. (2) and (4), the system is of high order and contains many control parameters. Thus, analyzing system performance is difficult. As such, the controller and system model have to be simplified first.

A. Simplified Controller and System Model

The quasi-PR controller shown in Eq. (4) can be rewritten as follows:

$$G_{PR}(s) = \frac{K_p}{n} \cdot \sum_{h=1}^{m} \frac{s^2 + 2\omega_c(1+K'_{ih})s + \omega_h^2}{s^2 + 2\omega_c s + \omega_h^2}, \qquad (7)$$

where $K'_{ih} = nK_{rh}/K_p$ is the relative resonant gain of the PR controller and n is the number of resonant controllers.

Fig. 5 shows the Bode diagram of the PR controller derived using Eq. (7) with different parameters. The following conclusions can be drawn: (1) K'_{ih} determines the relative gain at the target frequency ω_h. The gain gradually increases with the increase in K'_{ih}. However, the phase lag introduced by the controller is also increased. (2) ω_c mainly influences the resonant bandwidth at the target frequency to improve its robustness against the frequency fluctuation. (3) K_p shifts the magnitude plot up and down and has only a slight effect on the phase plot.

Based on Eq. (7), the gain at ω_h can be obtained as follows:

$$\left|G_{PR}(j\omega_h)\right| = (n+K'_{in})K_p/n. \qquad (8)$$

As shown in Fig. 5, the quasi-PR controller can be approximated to K_p at frequencies greater than ω_m, that is,

$$G_{PR}(j\omega) \approx K_p \quad \omega_m < \omega. \qquad (9)$$

Typically, the crossover angular frequency ω_{cs} is restricted to a value lesser than ω_{res}. Therefore, the LCL filter can be simplified as an L filter when calculating the magnitude at ω_{cs} and the frequencies lesser than ω_{cs}, which is also applicable for digitally controlled systems [8]. As such, the magnitude of $T(s)$

and $G_g(s)$ at ω_{cs} and the frequencies lesser than ω_{cs} can be simplified as follows:

$$|T(s)| \approx \left| \frac{G_{PR}(s)}{(L_1 + L_2)s} \right|, \quad (10)$$

$$|G_g(s)| \approx \left| \frac{1}{(L_1 + L_2)s} \right|. \quad (11)$$

Moreover, $|T(j\omega_{cs})| = 1$, combining Eqs. (9) and (10) produces the following equation:

$$K_p \approx \omega_{cs}(L_1 + L_2). \quad (12)$$

B. System Stability Constraint Condition Analysis

As analyzed previously, two RHP open-loop poles might be generated in $T(s)$ because of the delay effect. Thus, to ensure system stability, the Nyquist curve for positive frequency has to make one counterclockwise encirclement of the point $(-1, j_0)$. In the Nyquist diagrams of $T(s)$ shown in Fig. 6, the negative real axis crossings might occur at ω_{res} or at ω_{res} and $\omega_s/6$. Combining Eqs. (2), (9), and (12), the loop gain $T(s)$ at ω_{res} and $\omega_s/6$ can be obtained as follows:

$$T(j\omega_{res}) = -\frac{L_1 \omega_{cs}}{K}, \quad (13)$$

$$T(j\omega_s/6) = \frac{\omega_{res}^2 \omega_{cs}}{(\omega_s/6)^2} \frac{L_1}{K_c - K}. \quad (14)$$

From Eq. (13), we observed that the Nyquist curve of $T(s)$ always crosses over the negative real axis at ω_{res} for $K > 0$. As shown in Eq. (6), $K_c > 0$ for $\omega_{res} < \omega_s/6$ and $K_c \leq 0$ for $\omega_{res} \geq \omega_s/6$. Thus, if $\omega_{res} < \omega_s/6$, the Nyquist curve crosses over the negative real axis one more time at $\omega_s/6$ for $K > K_c$ [see Fig. 6(a)] and, if $\omega_{res} \geq \omega_s/6$, the Nyquist curve certainly crosses over the negative real axis at $\omega_s/6$ for $K > 0$ [see Fig. 6(b)]. We noted that, if $\omega_{res} = \omega_s/6$, the crossing points at ω_{res} and $\omega_s/6$ coincide with each other.

We assume the magnitude requirements of $T(s)$ at ω_{res} and $\omega_s/6$ are M_1 and M_2, respectively. Based on the previous analysis, the stability constraint condition on the grid current loop can be derived as follows:

1. If $0 < K < K_c$ when $\omega_{res} < \omega_s/6$, then no RHP open-loop pole exists in $T(s)$ and $|T(j\omega_{res})| \leq M_1 < 1$ is required to ensure that point $(-1, j_0)$ is not surrounded. Substituting Eq. (13) obtains the following equation:

$$\frac{L_1 \omega_{cs}}{M_1} \leq K < K_c. \quad (15)$$

Then, $\omega_{cs} < M_1 K_c / L_1$ is obtained. Substituting Eq. (6), the relationship between the crossover frequency $f_{cs} = \omega_{cs}/(2\pi)$ and f_{res} can be derived as follows:

$$\frac{f_{cs}}{f_s} < \frac{M_1}{6} \left[1 - \left(\frac{f_{res}}{f_s/6} \right)^2 \right]. \quad (16)$$

The sampling frequency f_s is typically at least twice that of the switching frequency f_{sw}. Based on Eq. (16), the curve of f_{cs} with the increase in f_{res} for $M_1 = 0.707$ is
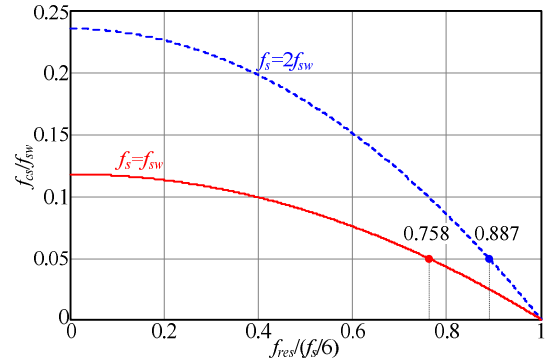

Fig. 7. Curves of f_{cs} with the increase in f_{res} for $M_1 = 0.707$.

depicted in Fig. 7. When f_{res} is close to $f_s/6$, f_{cs} decreases significantly. This finding implies that $K < K_c$ will not be suitable under this condition. However, to determine the response speed of the current loop and decouple the current loop with the outer voltage loop, f_{cs} should be at least 10 times that of the fundamental frequency f_1. Therefore, f_{res} should be less than 0.758 times of $f_s/6$ for $f_s = f_{sw} = 10$ kHz.

2. If $K > K_c$ when $\omega_{res} < \omega_s/6$, then two RHP open-loop poles exist in $T(s)$. Thus, $|T(j\omega_{res})| \leq M_1 < 1$ and $|T(j\omega_s/6)| \geq M_2 > 1$ are required. Then, the value range of K can be derived as follows:

$$\frac{L_1 \omega_{cs}}{M_1} \leq K \leq \frac{L_1 \omega_{cs}}{M_2} \left(\frac{\omega_{res}}{\omega_s/6} \right)^2 + \frac{L_1}{\omega_s/6} \left[(\omega_s/6)^2 - \omega_{res}^2 \right]. \quad (17)$$

3. If $K > 0$ when $\omega_{res} > \omega_s/6$, then two RHP open-loop poles always exist in $T(s)$, and $|T(j\omega_{res})| \geq M_1 > 1$ and $|T(j\omega_s/6)| \leq M_2 < 1$ are required. Then, the value range of K can be expressed as follows:

$$\frac{L_1 \omega_{cs}}{M_2} \left(\frac{\omega_{res}}{\omega_s/6} \right)^2 + \frac{L_1}{\omega_s/6} \left[(\omega_s/6)^2 - \omega_{res}^2 \right] \leq K \leq \frac{L_1 \omega_{cs}}{M_1}. \quad (18)$$

4. If $\omega_{res} = \omega_s/6$, then two RHP open-loop poles always exist in $T(s)$. However, the Nyquist curve is only tangent to the negative real axis and never crosses over, as shown in Fig. 6(b), which means that the system can hardly be stable irrespective of K.

C. Steady-state Error Analysis

As shown in Eq. (1), the grid current i_2 comprises two parts. One part is the command–current component generated by the current reference i_2^*. The other part is the voltage–current component generated by the grid voltage u_g. Based on Eq. (1), the grid current error can be derived as follows:

$$e(s) = i_2^*(s) - i_2(s) = \frac{1}{1 + T(s)} i_2^*(s) + \frac{G_g(s)}{1 + T(s)} u_g(s). \quad (19)$$

Considering the role of the controller, if the magnitude of $T(s)$ at the fundamental angular frequency ω_1 is sufficiently large, then $1 + T(j\omega_1) \approx T(j\omega_1)$. Moreover, as the influence of the filter capacitor is negligible at ω_1, considering Eqs. (1),
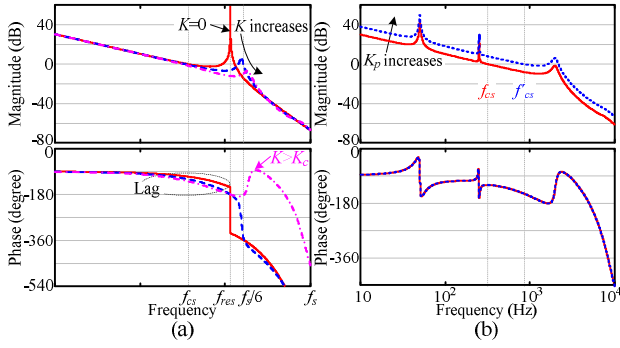
Fig. 8. Bode diagrams of the control objective $G_{LCL}(s)$ with different K (a) and the loop gain $T(s)$ with different K_p (b).

(10), and (11), the fundamental component of $i_2(s)$ can be approximated as follows:

$$i_2(j\omega_1) \approx i_2^*(j\omega_1) - \frac{u_g(j\omega_1)}{K_p + K_{r1}}. \tag{20}$$

As the quasi-PR controller can provide sufficiently large gain at ω_1, the voltage–current component could be attenuated to decrease its value, that is, $-u_g(j\omega_1)/(K_p + K_{r1}) \approx 0$. Thus, simplification of the steady-state error involves the amplitude error only, not the phase error. Moreover, as shown in Eq. (1), the harmonic currents are generated only by the grid harmonics. Therefore, the steady-state error requirement can be converted to the amplitude error requirements of the current components at ω_1 and ω_h, which are denoted by ε_i and ε_{uh}, respectively. Based on Eq. (19), ε_i and ε_{uh} are defined as follows:

$$\begin{cases} \varepsilon_i = \left| \dfrac{1}{1 + T(j\omega_1)} \right| \\ \varepsilon_{uh} = \left| \dfrac{G_g(j\omega_h)}{1 + T(j\omega_h)} \right| \end{cases}. \tag{21}$$

To ensure that the system is stable, ω_h should be lesser than ω_{cs}. Accordingly, substituting Eqs. (10) and (11) into Eq. (21), the relationship between the gain of the PR controller and steady-state amplitude errors can be approximated as follows:

$$|G_{PR}(j\omega_1)| \geq \max\left[\frac{1 - \varepsilon_i}{\varepsilon_i}(L_1 + L_2)\omega_1, \frac{1}{\varepsilon_{u1}} - (L_1 + L_2)\omega_1 \right], \tag{22}$$

$$|G_{PR}(j\omega_h)| \geq \frac{1}{\varepsilon_{uh}} - (L_1 + L_2)\omega_h \quad (h \neq 1). \tag{23}$$

Considering Eqs. (8) and (12), the relationship between K'_{ih} and the steady-state errors can be calculated as follows:

$$K'_{i1} \geq \max\left[\frac{1 - \varepsilon_i}{\varepsilon_i} \frac{n\omega_1}{\omega_{cs}} - n, \frac{n}{\varepsilon_{u1}\omega_{cs}(L_1 + L_2)} - \frac{n\omega_1}{\omega_{cs}} - n \right], \tag{24}$$

$$K'_{ih} \geq \frac{n}{\varepsilon_{uh}\omega_{cs}(L_1 + L_2)} - \frac{n\omega_h}{\omega_{cs}} - n \quad (h \neq 1). \tag{25}$$

D. Stability Margin Analysis

Based on the stability constraint condition analysis

discussed previously, we noted that the magnitude requirements M_1 and M_2 determine the GM of the system. Therefore, we focus on the PM only. As shown in Eq. (2), the PM is codetermined by the phases of the control object $G_{LCL}(s)$ and PR controller at ω_{cs}. The phase of $G_{LCL}(s)$ at ω_{cs} decreases with the increase in K [see Fig. 8(a)]. With respect to the PR controller, Fig. 5 shows that the phase lag caused by the PR controller increases with the increase in K'_{ih}. ω_c is relatively small. Thus, the effect of ω_c on the PM is disregarded. K_p has no effect on the phase response, but K_p affects ω_{cs}. Thus, the PM of the system is related to K, K'_{ih}, and K_p.

As analyzed previously, K regulates system stability and K'_{ih} influences steady-state error. Therefore, when system stability and steady-state error have been ascertained, the system phase response could be derived by using Eq. (2) with $K_p/n = 1$, and PM is related to K_p only. As shown in Fig. 8(b), the PM is changed with different values of ω_{cs}, which is approximately proportional to the value of K_p. As $|T(j\omega_{cs})| = 1$, substituting Eq. (9) into Eq. (2), the accurate relationship between K_p and ω_{cs} can be derived as follows:

$$K_p = \frac{\omega_{cs}(L_1 + L_2)}{\omega_{res}^2} \sqrt{\left[\omega_{res}^2 - \omega_{cs}^2 + \frac{K\omega_{cs}\sin(1.5T_s\omega_{cs})}{L_1} \right]^2 + \left[\frac{K\omega_{cs}\cos(1.5T_s\omega_{cs})}{L_1} \right]^2}. \tag{26}$$

V. DESIGN OF THE CURRENT CONTROLLER AND CAPACITOR–CURRENT–FEEDBACK COEFFICIENT

A. Design Procedure of the Control Parameters

As analyzed previously, the damping gain K mainly influences the system stability, the relative resonant gain K'_{ih} mainly regulates the steady-state error, and the proportional gain K_p mainly affects the PM of the system. Thus, a simplified controller design method based on the specifications of the current loop is proposed as follows:

Step 1. The specifications of the grid current loop are determined, specifically ε_i and ε_{uh} by the requirements of the steady-state errors at the target frequencies, the PM by the requirements of the dynamic response and robustness, and ω_{cs} by the requirement of the dynamic response speed.

As the fundamental voltage amplitude is greater than the harmonic voltages in the grid, ε_{u1} should be less than ε_{uh}. In general, PM in the range of (30°, 60°) is required for good dynamic response and robustness. However, when more resonant controllers are used, the PM requirement has to be reduced because PM significantly decreases with the increases in K'_{ih} and n. In [27], ω_{cs} is limited to less than 0.3 times that of ω_{res} to ensure
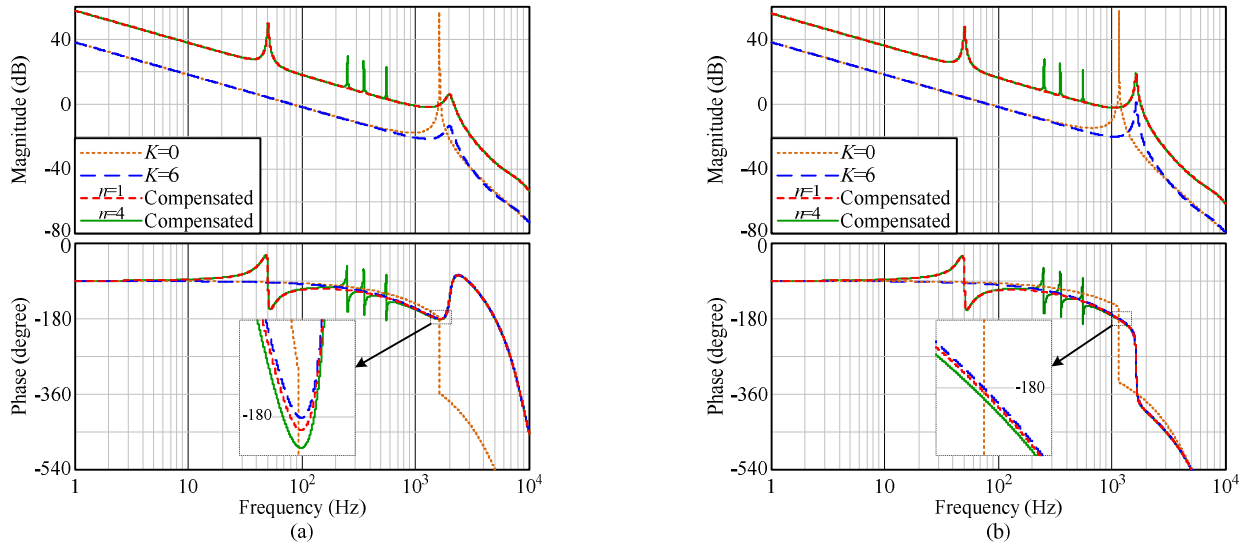
Fig. 9. Bode diagrams of the grid current loop before and after compensation with different controllers: (a) Case I and (b) Case II.

system-sufficient PM. However, considering the variation of ω_{res}, which will approach $\omega_s/3$ [10], because of the delay effect, the limit of ω_{cs} could be relaxed, especially for $\omega_{res} < \omega_s/3$. In general, ω_{cs} could be set at approximately $0.45\omega_{res}$. Moreover, ω_{cs} should be greater than the highest resonant frequency ω_m of the controller and lesser than $\omega_s/10$, that is, $\omega_s/10 > \omega_{cs} > \omega_m$.

Step 2. K is designed based on the stability requirement.

The value range of K can be obtained from Eq. (15), (17), or (18), which depends on ω_{res}. We noted that $M_x \geq 1.414$ ($x = 1, 2$) for $M_x > 1$ and $M_x \leq 0.8$ for $M_x < 1$ are required to ensure robust system stability. Then, we select a suitable value from the value range of K, with the compromise of dynamic performance and robustness.

Step 3. ω_c is designed based on the deviation range of the grid fundamental frequency.

Based on the definition of bandwidth, the difference of the two frequencies where the gain of the resonant part is equal to $K_{r1}/\sqrt{2}$ is the resonant bandwidth. Suppose that the maximum allowable deviation of the grid fundamental frequency is Δf, thus, $\omega_c = 2\pi\Delta f$ can be obtained.

Step 4. K_{ih}' is designed based on the steady-state error requirements.

Based on the requirements of the amplitude steady-state errors ε_i and ε_{uh}, K_{ih}' can be calculated from Eqs. (24) and (25). To ensure a larger system PM, K_{ih}' should have a smaller value.

Step 5. K_p is designed based on the PM requirement.

After the previous steps, the phase response of the system can be obtained by drawing the Bode plot of the loop gain $T(s)$ from Eqs. (2) and (7), with $K_p/n = 1$. We check the PM at the predesigned ω_{cs}. If the PM satisfies the requirement in Step 1, ω_{cs} remains unchanged; if not, a larger PM should be selected to ensure system stability with an acceptable ω_{cs}. Then, we calculate K_p from Eq. (26).

B. Design Example

Based on a 5 kW prototype in the laboratory, two different filter capacitor values are considered to range the filter resonance frequency. The parameters of the LCL-type PWM converter are given in TABLE I. We consider four resonant controllers ($h = 1, 5, 7, 11$). Given that f_{res} in Case I is close to $f_s/6$, $K > K_c$ is preferred rather than $K < K_c$. From [20], the maximum deviation of the grid fundamental frequency is approximately 0.5 Hz. As such, Δf is equal to 0.5 Hz in Step 3. The design procedures and results are shown in Table II, where GM_1 and GM_2 denote the GM around ω_{res} and $\omega_s/6$, respectively. The parameters of the quasi-PR controller corresponding to Eq. (4) are $K_p = 9.6$, $K_{r1} = 180$, and $K_{rh} = 84$ for Case I and $K_p = 7.8$, $K_{r1} = 146.25$, and $K_{rh} = 68.25$ for Case II.

Fig. 9 shows the Bode diagrams of the grid current loop before and after compensation with different controllers. By comparison, we observed that the phase lag introduced by the controller will shift the −180° crossing point, which could improve system robustness to a certain extent, especially for f_{res} close to $f_s/6$ when the active damping loop is unstable. Specifically, for Case I, the GM increases from $GM_1 = 0.898$ dB and $GM_2 = −0.782$ dB with one resonant controller ($n = 1$) to $GM_1 = 1.27$ dB and $GM_2 = −1.27$ dB with four resonant controllers ($n = 4$), but the PM decreases from 33.7° to 31.2°.
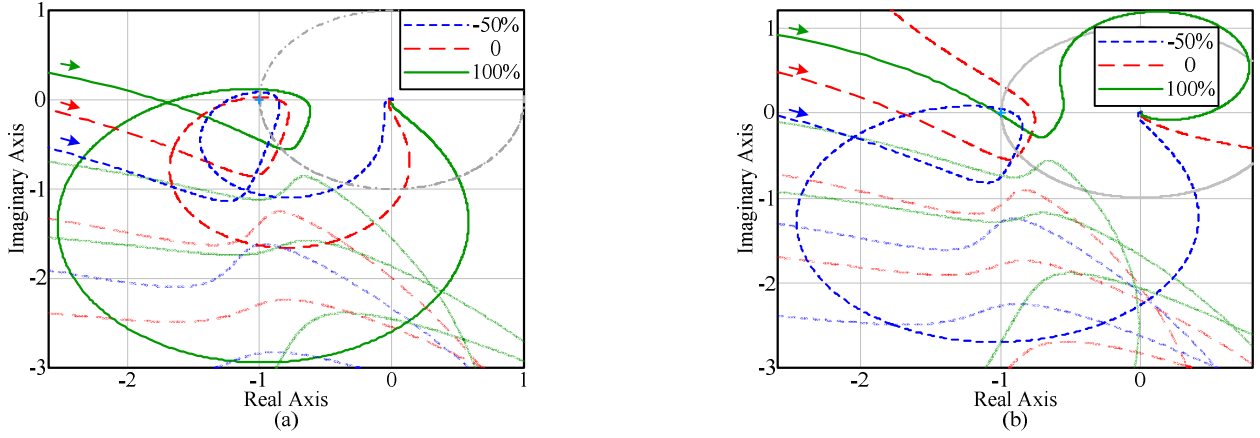
Fig. 10. Nyquist plots of the grid current loop around the critical point when L_2 changes from −50% to 50%: (a) Case I and (b) Case II.

For Case II, the GM increases slightly from 2.21 dB to 2.27 dB and the PM decreases from 34.1° to 29.3°. Moreover, considering the delay effect, we observed that the LCL resonant frequency deviates from ω_{res}. The actual resonant angular frequency ω'_{res} and the actual damping ratio ζ' are derived in the Appendix and expressed as follows:

$$\omega'_{res} = \left. \frac{\omega_{res}}{\sqrt{1 - K \sin(1.5T_s\omega)/(\omega L_1)}} \right|_{\omega=\omega'_{res}}, \qquad (27)$$

$$\zeta' = \left. \frac{K}{2L_1\omega_{res}} \frac{\cos(1.5T_s\omega)}{\sqrt{1 - K \sin(1.5T_s\omega)/(\omega L_1)}} \right|_{\omega=\omega'_{res}}. \qquad (28)$$

In Eq. (27), by letting $f(\omega) = 1/\sqrt{1 - K \sin(1.5T_s\omega)/(\omega L_1)}$, obtaining $\sin(1.5T_s\omega) > 0$, $f(\omega) > 1$ for $\omega < \omega_s/3$ and $\sin(1.5T_s\omega) < 0$, $f(\omega) < 1$ for $\omega > \omega_s/3$ becomes relatively easy. As a result, with the increase in K, ω'_{res} is greater than ω_{res} for $\omega_{res} < \omega_s/3$ and lesser than ω_{res} for $\omega_{res} > \omega_s/3$, but never exceeds $\omega_s/3$. This finding means that ω'_{res} will be close to $\omega_s/3$ with the increase in K. We noted that, for $K = K_c$, the active damping loop is marginally stable with $\omega_{pc} = \omega_s/6$ and has no contribution to the resonance damping, $\omega'_{res} = \omega_s/6$.

In the actual condition, L_1 and C do not significantly change, except for L_2 (considering the impact of grid impedance). Fig. 10 shows the Nyquist plots of the grid current loop around the critical point when L_2 is decreased by 50% or increased by 100%. This finding indicates that the grid current loop remains stable for both cases when L_2 is decreased by 50% or increased by 100%. Nevertheless, the PM of Case I changes from 23.9° to 33.3° [see Fig. 10(a)] and the PM of Case II changes from 26.6° to 2.07° [see Fig. 10(b)]. We noted that the GM decreases significantly for Cases I and II, and the active damping loop of Case II becomes unstable when L_2 is decreased by 50%. Thus, to improve system robustness, K should have a larger value in Step 2 when the active damping loop is stable.

TABLE I
LCL FILTER SYSTEM PARAMETERS

Nominal System Parameters		
Phase RMS: u_g = 50 V	f_1 = 50 Hz	C_{dc} = 1,880 µF
u_{dc} = 200 V	f_{sw} = 10 kHz	f_s = 10 kHz
L_1 = 1.2 mH	L_2 = 0.8 mH	T_s = 100 µs
Capacitances and Resonance Frequencies		
Case I	C = 20 µF	f_{res} = 1,624 Hz	$f_{res}/(f_s/6)$ = 0.9743
Case II	C = 40 µF	f_{res} = 1,149 Hz	$f_{res}/(f_s/6)$ = 0.6888

TABLE II
DESIGN PROCEDURE AND RESULTS

Design Steps	Case I		Case II		
	K_c = 0.635		K_c = 6.598		
	$f_{res}/(f_s/6)$ = 0.9743 > 0.758		$f_{res}/(f_s/6)$ = 0.6888 < 0.758		
Step 1	ε_i = 1%, ε_{u1} = 0.5%, and ε_{uh} = 1%; n = 4				
	PM ≥ 30° f_{cs} = 780 Hz		PM ≥ 30° f_{cs} = 500 Hz		
Step 2	M_1 = 0.99, M_2 = 1.01		M_1 = 0.707		
	5.94 ≤ K ≤ 6.161 → K = 6		5.332 ≤ K < 6.598 → K = 6		
Step 3	Δf = 0.5 Hz → $\omega_c = 2\pi\Delta f \approx 3$				
Step 4	$K'_{i1} \geq 75.327 \cdots K'_{i1} \geq 34.539$		$K'_{i7} = 34.039 \cdots K'_{i11} = 33.039$		
	$K'_{i1} = 75$		$K'_{ih} = 35$		
Step 5	f_{cs} = 800 Hz; K_p = 9.442		f_{cs} = 650 Hz; K_p = 7.844		
Design Results	K = 6	K_p = 9.6	K'_{i1} = 75	K = 6	K_p = 7.8	K'_{i1} = 75
	K'_{ih} = 35	f_{cs} = 819 Hz	PM = 31.2°	K'_{ih} = 35	f_{cs} = 650 Hz	PM = 29.3°
	GM$_1$ = 1.27 dB	GM$_2$ = −1.27 dB		GM = 2.27 dB		

VI. EXPERIMENTAL VERIFICATION

A 5 kW prototype has been constructed in the laboratory to verify the effectiveness of the proposed design method. The key parameters of the prototype are listed in TABLE I. A Yy-type galvanic isolation transformer is placed between the LCL-type PWM converter and the grid. The grid voltages and currents are sensed by voltage/current halls. The control
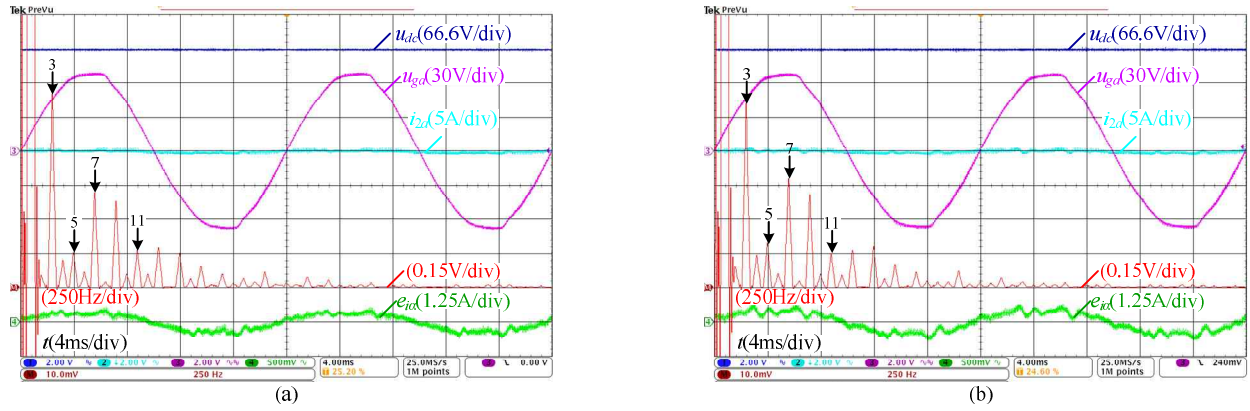
Fig. 11. Experimental waveforms at no load for (a) Case I and (b) Case II. From top to bottom: the DC link voltage u_{dc}, the grid voltage u_{ga}, the grid current i_{2a}, the spectrum of u_{ga}, and the current tracking error of α-axis $e_{i\alpha}$.
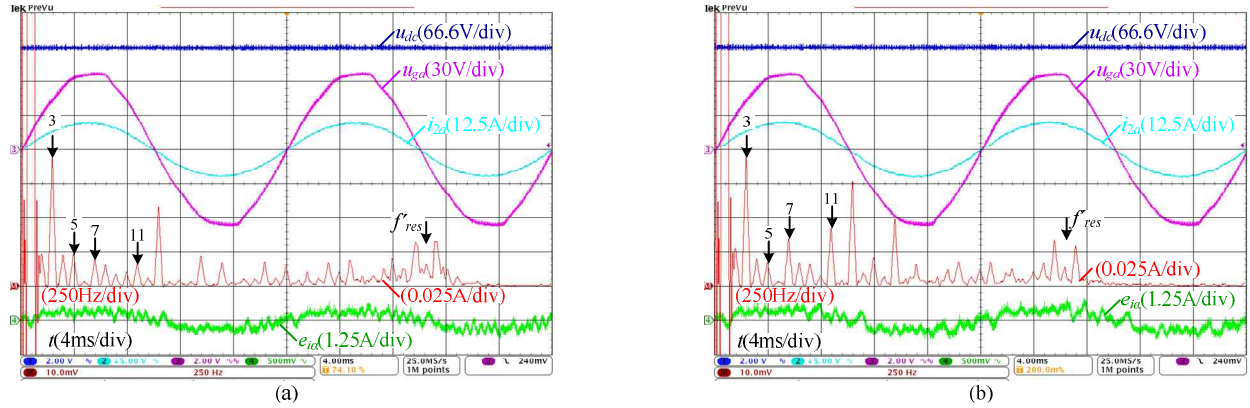

Fig. 12. Experimental waveforms with a DC resistant load $R = 40\ \Omega$ and PF set to 1.0 for (a) Case I and (b) Case II. From top to bottom: the DC link voltage u_{dc}, the grid voltage u_{ga}, the grid current i_{2a}, the spectrum of i_{2a}, and the current tracking error of α-axis $e_{i\alpha}$.
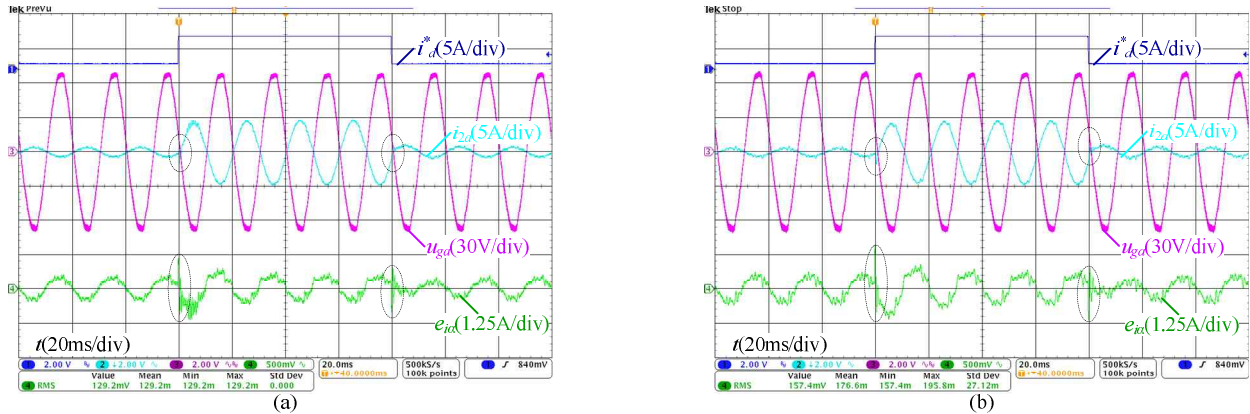

Fig. 13. Transient experimental results at inverter mode when the grid current reference ranges between 1 A and 5 A: (a) Case I and (b) Case II.

algorithm is implemented in a 32-bit float-point digital signal processor (TMS320F28335). The quasi-PR controller is discretized by Tustin transformation. In this study, the capacitor current is indirectly sensed through the difference between i_1 and i_2, and the current waveforms are inverted on the oscilloscope.

Fig. 11 shows the experimental waveforms at no load for Cases I and II, where the current tracking error of α-axis $e_{i\alpha}$ is measured through the analog-to-digital conversion interface

on the control board. From the spectra of u_{ga}, we observed that low-order harmonics exist in the real power grid, and the total harmonic distortion (THD) is 2.293%. The measured steady-state errors normalized with respect to u_g are listed in TABLE III. Considering the current distortion and the effect of dead time, the errors are slightly larger than the actual values of ε_{u1}, which are calculated from Eq. (21) using the designed parameters.

Fig. 12 shows the experimental waveforms when the DC

TABLE III
MEASURED RESULTS

Case	Actual ε_{u1} (%)	$e_{i\alpha}$ (%)		$R = 40\ \Omega$				
		No load	$R = 40\ \Omega$	5th	7th	11th	PF	THD
I	0.527	0.534	0.524	0.343%	0.290%	0.238%	0.999	2.031%
II	0.649	0.658	0.636	0.246%	0.473%	0.613%	0.998	2.351%

resistant load is 40 Ω, with power factor (PF) set to 1.0. We observed that the grid current is sinusoidal and the harmonics at the target frequencies (5th, 7th, and 11th) have been well suppressed. Moreover, the resonant peak is not dampened to less than 0 dB, which coincided with the design results. However, considering the leakage inductance of the isolation transformer, the actual resonant frequency f'_{res} is slightly lesser than the theoretical value shown in Fig. 9. The actual resonant frequencies are approximately 1,900 Hz for Case I and 1,650 Hz for Case II. The measured error $e_{i\alpha}$, PF, and harmonic contents at the target frequencies are listed in TABLE III. The measured errors are 0.524% for Case I and 0.636% for Case II, which are slightly smaller than that at no load because the command–current error ε_i at rectifier mode can cancel some of the voltage–current error ε_{u1}, which can be observed in Eq. (19) when the direction of current i_2 at inverter mode is positive in the actual system. Given that the gain at ω_1 for Case I is larger than that for Case II, the measured error and PF for Case I are slightly smaller than that for Case II.

To evaluate dynamic performance, the LCL-type PWM converter operating without the outer voltage loop is used. The DC link voltage is provided by a three-phase noncontrolled rectifier. Fig. 13 shows the transient experimental results when the grid current reference i_d^* ranges between 1 A and 5 A for Cases I and II with PF set to 1.0. We observed that the inverters rapidly responded to the reference change and the current tracking error of α-axis $e_{i\alpha}$ is sustained at approximately zero all the time. Nevertheless, oscillation occurs during the current step change because the resonant peaks are not dampened to less than 0 dB, which implies that the actual damping ratios are small because of the delay effect. Based on Eq. (28), the actual damping ratio ζ' can be calculated at approximately 0.07 for Case I and 0.01 for Case II.

VII. CONCLUSIONS

In this study, we analyzed the characteristics and controller design method for the digitally controlled LCL-type PWM converter based on the multi-resonant quasi-PR controller and capacitor–current–feedback active damping. The effect of the delay on the active damping performance is investigated by using the Nyquist diagrams. If the damping loop is unstable, two RHP open-loop poles are generated in the grid current loop, which is codetermined by the LCL resonant frequency (f_{res}) and the active damping gain (K). Then, the system stability constraint condition can be obtained based on the

Nyquist stability criterion. Moreover, impact analysis of the control parameters on the current loop performance identifies that different control parameters play different decisive roles in the current loop performance: K mainly influences the system stability, the relative resonant gain mainly regulates the steady-state error, and the proportional gain mainly affects the PM of the system. Based on the analysis, a simplified controller design method based on the system specifications is proposed. The proposed method can obtain the optimum controller, which ensures system stability with high robustness and strong ability to suppress the effect of the grid voltage low-order harmonics. Following the method, two design examples are given and the design results are directly used on a laboratory prototype. The experimental results are consistent with the design specifications. These findings confirm the practicability and operability of the proposed design method.

APPENDIX

From Eq. (2), the denominator of $T(s)$ can be obtained as follows:

$$Den(s) = (L_1 + L_2)s\left[s^2 + se^{-1.5T_s s}K/L_1 + \omega_{res}^2\right]. \quad (29)$$

Based on Euler's formula, the delay element $e^{-1.5T_s s}$ can be written in the frequency domain, that is,

$$e^{-j1.5T_s\omega} = \cos(1.5T_s\omega) - j\omega\cdot\sin(1.5T_s\omega)/\omega. \quad (30)$$

Applying $s = j\omega$ to Eq. (30) obtains $e^{-1.5T_s s} = \cos(1.5T_s\omega) - \sin(1.5T_s\omega)s/\omega$. Substituting this formula into Eq. (29) enables us to rewrite $Den(s)$ into the form $Den(s) = As\left(s^2 + 2\zeta'\omega'_{res}s + \omega'^2_{res}\right)$. Then, the actual resonant angular frequency ω'_{res} and the actual damping ratio ζ' are derived as follows:

$$\omega'_{res} = \frac{\omega_{res}}{\sqrt{1 - K\sin(1.5T_s\omega)/(\omega L_1)}}\Bigg|_{\omega=\omega'_{res}}, \quad (31)$$

$$\zeta' = \frac{K}{2L_1\omega_{res}}\frac{\cos(1.5T_s\omega)}{\sqrt{1 - K\sin(1.5T_s\omega)/(\omega L_1)}}\Bigg|_{\omega=\omega'_{res}}, \quad (32)$$

where $A = (L_1 + L_2)\left[1 - K\sin(1.5T_s\omega)/(\omega L_1)\right]$.

Substituting $\omega = \omega'_{res}$ into Eq. (31) and solving the equation by using a mathematical software, ω'_{res} can be calculated. The curve of the function $f(x)$ calculated by using Eq. (33) can be illustrated. The value of the point that intersects the x-axis is the actual resonant angular frequency.

$$f(x) = x - \frac{\omega_{res}}{\sqrt{1 - K\sin(1.5T_s x)/(xL_1)}} \quad (33)$$

REFERENCES

[1] S. Vazquez, S. M. Lukic, E. Galvan, L. G. Franquelo, and J. M. Carrasco, "Energy storage systems for transport and grid applications," *IEEE Trans. Ind. Electron.,* Vol. 57, No. 12, pp. 3881-3895, Dec. 2010.

[2] B. Singh, B. N. Singh, A. Chandra, K. Al-Haddad, A. Pandey, and D. P. Kothari, "A review of three-phase improved power quality AC-DC converters," *IEEE Trans. Ind. Electron.,* Vol. 51, No. 3, pp. 641-660, Jun. 2004.

[3] S. Tang, L. Peng, and Y. Kang, "Active damping method using Grid-Side current feedback for active power filters with LCL filters," *Journal of Power Electronics,* Vol. 11, No. 3, pp. 311-318, Mar. 2011.

[4] G. Hu, C. Chen, and D. Shanxu, "New active damping strategy for LCL-Filter-Based Grid-Connected inverters with harmonics compensation," *Journal of Power Electronics,* Vol. 13, No. 2, pp. 287-295, Mar. 2013.

[5] J. He and Y. Li, "Generalized closed-loop control schemes with embedded virtual impedances for voltage source converters with LC or LCL filters," *IEEE Trans. Power Electron.,* Vol. 27, No. 4, pp. 1850-1861, Apr. 2012.

[6] L. Zhou, M. Yang, Q. Liu, and K. Guo, "New control strategy for three-phase grid-connected LCL inverters without a phase-locked loop," *Journal of Power Electronics,* Vol. 13, No. 3, pp. 487-496, May 2013.

[7] S. G. Parker, B. P. McGrath, and D. G. Holmes, "Regions of active damping control for LCL filters," *IEEE Trans. Ind. Appl.,* Vol. 50, No. 1, pp. 424-432, Jan./Feb. 2014.

[8] C. Bao, X. Ruan, X. Wang, W. Li, D. Pan, and K. Weng, "Design of injected grid current regulator and capacitor-current-feedback active-damping for LCL-type grid-connected inverter," in *Proc. IEEE Energy Conversion Congress and Exposition (ECCE)*, pp. 579-586, 2012.

[9] C. Bao, X. Ruan, X. Wang, W. Li, D. Pan, and K. Weng, "Step-by-step controller design for LCL-type grid-connected inverter with capacitor–current-feedback Active-Damping," *IEEE Trans. Power Electron.,* Vol. 29, No. 3, pp. 1239-1253, Mar. 2014.

[10] D. Pan, X. Ruan, C. Bao, W. Li, and X. Wang, "Capacitor-Current-Feedback active damping with reduced computation delay for improving robustness of LCL-Type Grid-Connected inverter," *IEEE Trans. Power Electr.,* Vol. 29, No. 7, pp. 3414-3427, Jul. 2014.

[11] S. Buso and P. Mattavelli, *Digital Control in Power Electronics*, Morgan & Claypool, pp. 17-66, 2006.

[12] D. G. Holmes, T. A. Lipo, B. McGrath, and W. Y. Kong, "Optimized design of stationary frame three phase AC current regulators," *IEEE Trans. Power Electron.,* Vol. 11, No. 24, pp. 2417-2426, Nov. 2009.

[13] X. Zhang, J. W. Spencer, and J. M. Guerrero, "Small-signal modeling of digitally controlled Grid-Connected inverters with LCL filters," *IEEE Trans. Ind. Electron.,* Vol. 60, No. 9, pp. 3752-3765, Sep. 2013.

[14] M. Liserre, R. Teodorescu, and F. Blaabjerg, "Multiple harmonics control for three-phase grid converter systems with the use of PI-RES current controller in a rotatiing frame," *IEEE Trans. Power Electron.,* Vol. 21, No. 3, pp. 836-841, May 2006.

[15] C. Lascu, L. Asiminoaei, I. Boldea, and F. Blaabjerg, "High performance current controller for selective harmonic compensation in active power filters," *IEEE Trans. Power Electron.,* Vol. 22, No. 5, pp. 1826-1835, Sep. 2007.

[16] A. G. Yepes, F. D. Freijedo, O. Lopez, and J. Doval-Gandoy, "Analysis and design of resonant current controllers for voltage-source converters by means of nyquist diagrams and sensitivity function," *IEEE Trans. Ind. Electron.,* Vol. 58, No. 11, pp. 5231-5250, Nov. 2011.

[17] A. G. Yepes, F. D. Freijedo, O. Lopez, and J. Doval-Gandoy, "High- performance digital resonant controllers implemented with two integrators," *IEEE Trans. Power Electron.,* Vol. 26, No. 2, pp. 563-576, Feb. 2011.

[18] D. N. Zmood and D. G. Holmes, "Stationary frame current regulation of PWM inverters with zero steady-state error," *IEEE Trans. Power Electron.,* Vol. 18, No. 3, pp. 814-822, May 2003.

[19] R. Teodorescu, F. Blaabjerg, M. Liserre, and P. C. Loh, "Proportional-resonant controllers and filters for grid-connected voltage-source converters," *IEE Proc. Electric Power Applications,* Vol. 153, No. 5, pp. 750-762, Sep. 2006.

[20] *IEEE Recommended practice for utility interface of photovoltaic (PV) systems*, IEEE Standard 929, 2000.

[21] M. Castilla, J. Miret, J. Matas, L. G. de Vicuna, and J. M. Guerrero, "Control design guidelines for single-phase grid-connected photovoltaic inverters with damped resonant harmonic compensators," *IEEE Trans. Ind. Electron.,* Vol. 56, No. 11, pp. 4492-4501, Nov. 2009.

[22] M. Castilla, J. Miret, J. Matas, L. G. de Vicuna, J. M. Guerrero, and T. Abeyasekera, "Linear current control scheme with series resonant harmonic compensator for single-phase grid-connected photovoltaic inverters," *IEEE Trans. Ind. Electron.,* Vol. 55, No. 7, pp. 2724-2733, Jul. 2008.

[23] Y. Huacheng, L. Hua, L. Yongcan, L. Yong, and W. Xingwei, "A multi-resonant PR inner current controller design for reversible PWM rectifier," in *Proc. IEEE Applied Power Electronics Conference and Exposition (APEC)*, pp. 316-320, 2013.

[24] B. Li, M. Zhang, L. Huang, L. Hang, and L. M. Tolbert, "A robust multi-resonant PR regulator for three-phase grid-connected VSI using direct pole placement design strategy," in *Proc. IEEE Applied Power Electronics Conference and Exposition (APEC)*, pp. 960-966, 2013.

[25] P. Rodriguez, J. Pou, J. Bergas, J. I. Candela, R. P. Burgos, and D. Boroyevich, "Decoupled double synchronous reference frame PLL for power converters control," *IEEE Trans. Power Electron.,* Vol. 22, No. 2, pp. 584-592, Mar. 2007.

[26] I. J. Gabe, V. F. Montagner, and H. Pinheiro, "Design and implementation of a robust current controller for VSI connected to the grid through an LCL filter," *IEEE Trans. Power Electron.,* Vol. 24, No. 6, pp. 1444-1452, Jun. 2009.

[27] Y. Tang, P. Loh, P. Wang, F. Choo, and F. Gao, "Exploring inherent damping characteristic of LCL-filters for three-phase grid-connected voltage source inverters," *IEEE Trans. Power Electron.,* Vol. 27, No. 3, pp. 1433-1443, Mar. 2012.

Yongcan Lyu was born in Hubei province, China, in 1985. He received his B.E. degree in Automation from Northeastern University, Shenyang, China, in 2007 and his M.S. degree in Thermal Engineering from Huazhong University of Science and Technology (HUST), Wuhan, China, in 2009. He is currently working toward his Ph.D. degree in Electrical Engineering at the School of Electrical and Electronic Engineering, HUST, Wuhan, China. His current research interests

include digital control technique and battery energy storage systems.

Hua Lin was born in Wuhan, China, in 1963. She received her B.S. degree in Industrial Automation from Wuhan University of Technology, Wuhan, China, in 1984; her M.S. degree in Electrical Engineering from Naval University of Engineering, Wuhan, China, in 1987; and her Ph.D. degree in Electrical Engineering from Huazhong University of Science and Technology (HUST), Wuhan, China, in 2005. From 1987 to 1999, she was with the Department of Electrical Engineering, Naval University of Engineering, as a lecturer and associate professor. Since 1999, she has been with the School of Electrical and Electronic Engineering, HUST, where she became a full professor in 2005. From October 2010 to April 2011, she has been a visiting scholar with the Center for Advanced Power Systems, Florida State University, Tallahassee, FL, USA. She has been engaged in research and teaching in the field of power electronics and electrical drives. Her research interests include high-power, high-performance AC motor drives, novel power converters, and their control. She has authored or coauthored more than 30 technical papers in journals and conferences. Dr. Lin received the second-grade National Scientific and Technological Advance Prize of China in 1996 and 2003.